Dynamic Nanocatalysis
https://www.sciltp.com/journals/dn

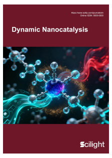

Article

Tuning Oxygen Vacancies in δ-MnO_2 by the *In-Situ* Modification of $CaSn(OH)_6$ to Enhance Formaldehyde Catalytic Oxidation Activity at Room Temperature

Ruimei Fang [1,*], Quanlin Li [1], Guoxin Lv [1], Xiaoai Luo [1], Hao Ma [2,*] and Haibao Huang [3]

[1] College of Environment and Resources, Chongqing Technology and Business University, Chongqing 400067, China
[2] Institute for Frontier Interdisciplinary Research in Intelligence and Environment, School of Big Data, Chongqing Technology and Business University, Chongqing 400067, China
[3] College of Ecology and Environment, Xinjiang University, Wulumuqi 830046, China
* Correspondence: fangruimei@126.com (R.F.); mahaoke@126.com (H.M.)

How To Cite: Fang, R.; Li, Q.; Lv, G.; et al. Tuning Oxygen Vacancies in δ-MnO_2 by the *In-Situ* Modification of $CaSn(OH)_6$ to Enhance Formaldehyde Catalytic Oxidation Activity at Room Temperature. *Dynamic Nanocatalysis* **2026**, *1*(1), 4. https://doi.org/10.53941/dn.2026.100004

Received: 24 March 2026
Revised: 19 May 2026
Accepted: 25 May 2026
Published: 3 June 2026

Abstract: The efficient elimination of indoor formaldehyde (HCHO) at room temperature continues to be a challenge, particularly under moisture-deficient conditions where conventional catalysts often suffer from rapid deactivation. In this work, a mild *in-situ* modification strategy using $CaSn(OH)_6$ was developed to engineer oxygen vacancies within layered δ-MnO_2, significantly enhancing its catalytic robustness. The optimized catalyst (MCS-1) exhibited superior HCHO oxidation performance, maintaining a high removal efficiency of 95% for over 260 min. Crucially, the catalyst demonstrated exceptional tolerance to low-humidity environments (RH = 20%), retaining >95% efficiency for 180 min, substantially outperforming pristine δ-MnO_2. The characterization results of XPS and EPR reveal that $CaSn(OH)_6$ incorporation facilitates the formation of oxygen vacancies. The shift of the lattice oxygen desorption peak to a lower temperature in the TPD results indicates that the modification by $CaSn(OH)_6$ enhances the mobility of lattice oxygen. This synergistic effect promotes the activation of molecular oxygen and facilitates the rapid desorption of carbonate intermediates, thereby preventing active site blocking. This work provides a promising defect-engineering strategy for designing high-performance manganese-based catalysts tailored for harsh indoor environments.

Keywords: catalytic oxidation; formaldehyde; δ-MnO_2; oxygen vacancies; $CaSn(OH)_6$ modification

1. Introduction

Formaldehyde (HCHO), a familiar volatile organic compound (VOC) derived from furniture and decoration materials [1,2], has been identified as a primary carcinogen by the IARC, posing severe and long-term risks to public health [3,4]. Among the various remediation technologies, catalytic oxidation is widely known as the most promising strategy for indoor air purification due to its complete mineralization of HCHO into CO_2 and H_2O under ambient conditions [5–7]. While noble metal catalysts (e.g., Pt, Pd, Ru) exhibit exceptional turnover frequencies at room temperature [8–11], their scarcity and prohibitive cost impede large-scale commercial application. Consequently, transition metal oxides have emerged as cost-effective alternatives [12–15]. In particularly, layered δ-MnO_2 has garnered significant attention owing to its unique 2D lamellar structure, large specific surface area, and abundant redox couples (Mn^{3+}/Mn^{4+}), which are favorable for catalytic reactions [16–18]. However, pristine δ-MnO_2 often suffers from sluggish kinetics and rapid deactivation, necessitating further structural optimization to meet the stringent requirements of practical application.

A critical yet frequently underestimated factor influencing catalytic performance is environmental humidity. Water molecules play a complex “double-edged” role in the HCHO oxidation mechanism. Under moderate humidity (e.g., RH = 50%), water dissociates on the catalyst surface to replenish surface hydroxyl groups (-OH), which are essential for mineralizing formate intermediates [19]. Conversely, excessive humidity leads to catalyst poisoning via the rival adsorption of water molecules on active sites [20]. More importantly, in low-humidity or arid environments, the catalytic cycle often collapses. The scarcity of external water vapor hinders the regeneration of surface hydroxyls, causing stubborn intermediates (e.g., dioxymethylene, formate, and carbonate) to accumulate and block the active sites. Therefore, developing robust catalysts that can sustain high activity under moisture-deficient conditions by reducing their dependence on external water is a significant challenge for indoor air quality control.

To overcome the limitations imposed by humidity, defect engineering—specifically the introduction of oxygen vacancies (Vo)—has proven to be an effective tactic [21–24]. Oxygen vacancies demonstrate pivotal influence in the Mars-van Krevelen mechanism: they not only serve as active sites for the adsorption of reactants (HCHO and O_2) but also act as electron donors to activate molecular oxygen into reactive surface oxygen species (e.g., O_2^- and O^-) [25]. Furthermore, a high concentration of oxygen vacancies can significantly enhance the mobility of lattice oxygen, accelerating its migration from the bulk to the surface [26]. Theoretically, a catalyst endowed with high lattice oxygen mobility can spontaneously replenish surface active oxygen consumed during the reaction, thereby maintaining the oxidative cycle and promoting the desorption of intermediates even without ample external moisture.

In this study, we present a facile strategy to tune the oxygen vacancies and surface electronic structure of δ-MnO_2 via *in-situ* modification with $CaSn(OH)_6$. Unlike simple physical mixing, the *in-situ* incorporation of $CaSn(OH)_6$ during hydrothermal synthesis induces significant lattice distortions and a high density of oxygen vacancies within the δ-MnO_2 framework. Comprehensive characterizations (XRD, Raman, XPS, H_2-TPR, and O_2-TPD) were employed to systematically investigate the structure-activity relationship. Moreover, *in-situ* DRIFTS technology was utilized to dynamically monitor the reaction pathway, revealing that the engineered oxygen vacancies accelerate the decomposition of carbonate intermediates. The optimized catalyst, MCS-1, exhibited superior durability and efficiency, maintaining over 95% HCHO removal efficiency even under low-humidity conditions (RH = 20%). This work provides new insights into designing moisture-tolerant manganese-based catalysts for robust indoor environment remediation.

2. Experimental Section

2.1. Catalysts Preparation

All reagents were analytical grade and used without any further pretreatment. The $CaSn(OH)_6$ microcubes were synthesized via a facile co-precipitation method. Briefly, NaOH (0.48 g) and $SnCl_4•5H_2O$ (0.7 g) were dissolved in deionized water (50 mL) to form a homogeneous solution. Subsequently, a $CaCl_2$ aqueous solution (0.222 g in 4 mL deionized water) was added dropwise into the above mixed solution under vigorous stirring. After continuous stirring for 4 h, the consequent white precipitate was gained by centrifugation, washed entirely with deionized water, and dried at 80 °C overnight. The pristine δ-MnO_2 (denoted as MnO_2-b) was prepared using a hydrothermal redox route with $KMnO_4$ and $MnSO_4•H_2O$ (molar ratio = 6:1). Typically, the $MnSO_4$ solution was added dropwise into the $KMnO_4$ solution. After stirring for 60 min, the admixture was transferred to a 100 mL Teflon-lined stainless steel autoclave and heated at 160 °C for 12 h. The final product was filtered, washed, and dried at 80 °C for 12 h. For the *in-situ* modified catalyst (MCS-1), a specific amount of as-prepared $CaSn(OH)_6$ (10 mol% relative to Mn) was dispersed into the mixed precursor solution prior to the hydrothermal treatment, following the same procedure as MnO_2-b. For comparison, a physically mixed sample (MCS-2) was obtained by mechanically grinding MnO_2-b with 10 mol% $CaSn(OH)_6$ in a mortar.

2.2. Catalysts Characterization

The crystalline structures were analyzed by X-ray diffraction (XRD) diffractometer (Rigaku D/max RA) employing Cu Kα radiation in the 2θ range of 10–80°. Raman spectra were recorded on a Renishaw InVia laser micro-Raman spectrometer with a 532 nm excitation laser (100–1000 cm). The morphology and microstructure were inspected using scanning electron microscopy (SEM, FEI Quanta 400 FEG) and transmission electron microscopy (TEM, FEI Tecnai G2 F20). Surface chemical states were determined by X-ray photoelectron spectroscopy (XPS) using a Thermo Fisher ESCALAB 250 spectrometer equipped with a monochromatic Al Kα X-ray source. Defects were characterized by Electron Paramagnetic Resonance (EPR) spectroscopy on a Bruker A300-10/12 spectrometer.

Redox properties were evaluated via H_2-temperature-programmed reduction (H_2-TPR) and O_2-temperature-programmed desorption (O_2-TPD) on a Micromeritics Auto Chem II 2920 analyzer. For H_2-TPR, the sample (0.5 g) was pretreated in a He flow at 200 °C for 60 min, cooled to room temperature, and then heated to 800 °C (10 $°C\cdot min^{-1}$) in a reducing H_2 atmosphere. For O_2-TPD, the sample was pretreated in He at 300 °C for 60 min, saturated with O_2 at 40 °C for 30 min, and purged with He to remove physically adsorbed species. The desorption profile was recorded from 40 to 900 °C at a ramp rate of 10 $°C\cdot min^{-1}$ under a He flow.

2.3. Catalytic Activity Evaluation

The catalytic oxidation reaction of HCHO was evaluated in a continuous-flow fixed-bed quartz reactor at 30 °C. 0.3 g of sample was loaded in the reactor. The reactant gas mixture consisted of 80 ppm HCHO, water vapor, and synthetic air (balance gas), with a total flow rate of 600 mL min^{-1}. This corresponded to a weight hourly space velocity (WHSV) of 120,000 $mL\cdot g^{-1}\cdot h^{-1}$. The gas flow rate was calculated at room temperature. The relative humidity (RH) was maintained at 50% using a water bubbler system, unless otherwise specified. Real-time HCHO concentrations were monitored using a high-precision photoacoustic multi-gas analyzer (GASERA ONE, Turku, Finland). The HCHO removal efficiency (η) was calculated using Equation (1):

$$\eta=\frac{C_{in}-C_{out}}{C_{in}}\times 100\% \tag{1}$$

where C_{in} and C_{out} represent the inlet and outlet HCHO concentrations, respectively. To assess durability, the stability of the optimized MCS-1 catalyst was tested over four consecutive cycles. Furthermore, the water tolerance of the catalysts was examined by varying the relative humidity to low (20%) and high (80%) levels.

2.4. In-Situ DRIFTS Measurements

In-situ diffuse reflectance infrared Fourier transform spectroscopy (DRIFTS) was employed to elucidate the reaction mechanism and identify surface intermediates. Spectra were recorded on a Bruker TENSOR II FT-IR spectrometer equipped with a liquid-nitrogen-cooled MCT detector and a Harrick *in-situ* reaction cell. Prior to the measurement, the catalyst was pretreated in a He flow at room temperature for 60 min to remove adsorbed impurities. Subsequently, a gas mixture containing 80 ppm HCHO was introduced into the cell. Time-resolved spectra were collected in the range of 650–4000 cm^{-1} with a resolution of 8 cm^{-1} and an accumulation of 16 scans.

3. Results and Discussion

3.1. Microstructure and Morphology Analysis

The crystallographic structures of the as-synthesized catalysts were first investigated by XRD (Figure 1a). The diffraction pattern of pristine MnO_2-b can be well-indexed to the birnessite-type δ-MnO_2 phase (JCPDS 80-1098), characterized by four diffraction peaks at 12.3°, 24.7°, 36.6°, and 66.1°, corresponding to the (001), (002), (110), and (020) crystal planes, respectively [27]. For the *in-situ* modified MCS-1 sample, the diffraction pattern retains the characteristic features of δ-MnO_2, suggesting that the layered structure is preserved. Interestingly, the intensity of the (001) peak in MCS-1 is noticeably enhanced compared to MnO_2-b, implying that the incorporation of $CaSn(OH)_6$ may induce a preferred orientation or expose more (001) facets during crystal growth. In contrast, the physically mixed MCS-2 sample displays additional peaks at 18.9°, 21.9°, and 31.1°, which are readily assigned to the cubic $CaSn(OH)_6$ phase (JCPDS 09-0030) [28], confirming the coexistence of two separate phases.

Raman spectroscopy was employed to probe the local atomic environment and structural disorder (Figure 1b). The spectrum of MnO_2-b exhibits three distinct bands at 498, 572, and 636 cm^{-1}. The dominant peak at 572 cm^{-1} is attributed to the stretching vibration of Mn–O bonds within the basal plane of [MnO_6] octahedra, while the band at 636 cm^{-1} corresponds to the symmetric stretching vibration of MnO_6 octahedra perpendicular to the layers [29]. Crucially, compared to MnO_2-b, the MCS-1 sample exhibits a significant broadening of the peak at 572 cm^{-1}. This peak broadening, often associated with a larger full width at half maximum (FWHM = 157.2), is a strong indicator of lattice disorder and symmetry breaking induced by the presence of oxygen vacancies or lattice defects [30]. This result suggests that the *in-situ* modification strategy effectively disrupts the long-range order of the Mn–O lattice, creating abundant structural defects

To quantitatively validate the existence of oxygen vacancies, Electron Paramagnetic Resonance (EPR) measurements were conducted (Figure 1c). All samples display a characteristic symmetrical EPR signal at $g \approx 2.003$, which originates from the unpaired electrons trapped in oxygen vacancies [31]. The signal intensity, which is directly proportional to the vacancy concentration, follows the order: MCS-1 > MCS-2 > MnO_2-b. The strongest

EPR signal observed for MCS-1 confirms that the *in-situ* introduction of $CaSn(OH)_6$ is far more effective than physical mixing in promoting the formation of surface oxygen vacancies. These abundant vacancies are expected to serve as active sites for oxygen activation in the subsequent catalytic process.

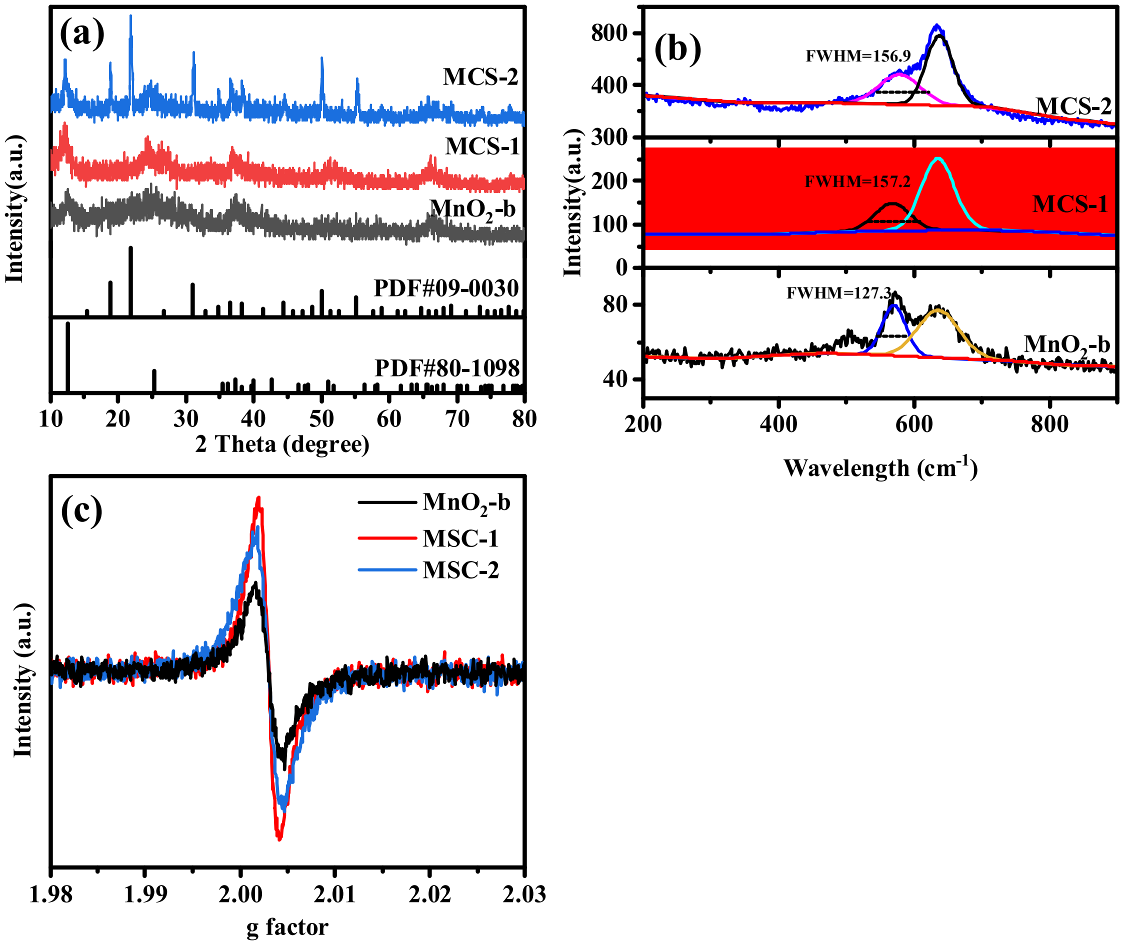

Figure 1. (**a**) XRD patterns, (**b**) Raman spectra and (**c**) EPR profiles of different catalysts.

The morphology and microstructure were visualized by SEM and TEM. As shown in Figure 2, both MnO_2-b and MCS-1 exhibit a hierarchical flower-like architecture assembled from ultrathin nanosheets. In the SEM images of MCS-1 (Figure 2c,d), no isolated $CaSn(OH)_6$ particles are detected, indicating that the $CaSn(OH)_6$ nanocubes are uniformly encapsulated within the δ-MnO_2 nanosheets. This "wrapping" structure maximizes the interfacial contact between the two components. Conversely, the MCS-2 sample (Figure 2e,f) shows a chaotic aggregation of δ-MnO_2 nanoflowers and exposed $CaSn(OH)_6$ cubes, typical of a physically mixed composite.

Transmission Electron Microscopy (TEM) provides deeper insight into the lattice structure (Figure 3). The nanosheet assembly of the nanoflowers is clearly visible in all samples. High-resolution TEM (HRTEM) images reveal distinct lattice fringes with an interplanar spacing of 0.64 nm, corresponding to the (001) plane of layered δ-MnO_2. However, a closer inspection of the MCS-1 lattice (Figure 3f) reveals significant lattice distortions, discontinuities, and amorphous regions within the crystal domains. These features act as visual evidence of the lattice strain and defects caused by the *in-situ* modification [25,32]. Such structural imperfections are highly favorable for catalysis as they facilitate the mobility of lattice oxygen. In contrast, the MCS-2 sample (Figure 3i) clearly displays the simultaneous presence of δ-MnO_2 (0.64 nm) and $CaSn(OH)_6$ ((220) plane, 0.286 nm) lattice fringes [33], further confirming the formation of a heterojunction in the physically mixed sample.

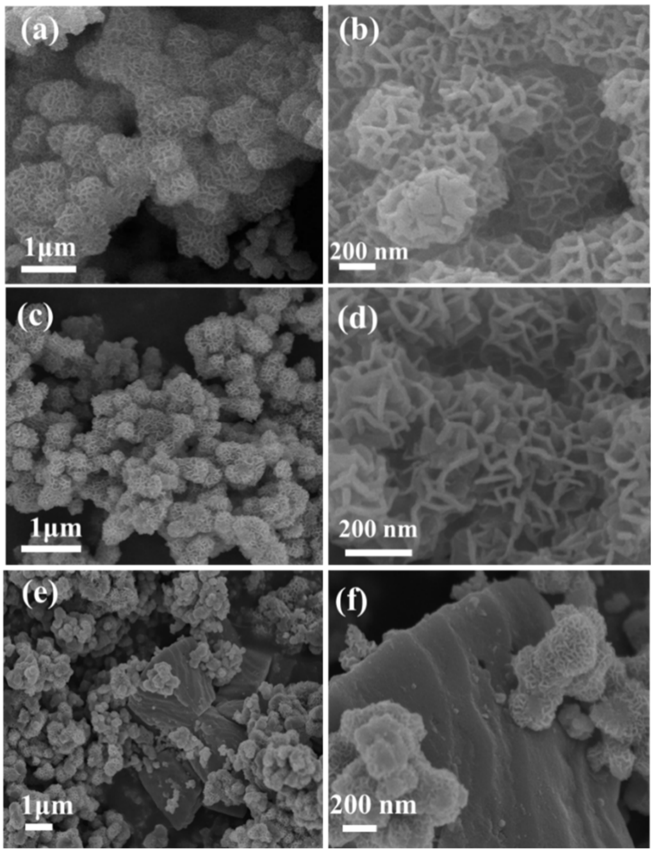

Figure 2. SEM images of (**a**,**b**) MnO_2-b, (**c**,**d**) MCS-1 and (**e**,**f**) MCS-2 samples.

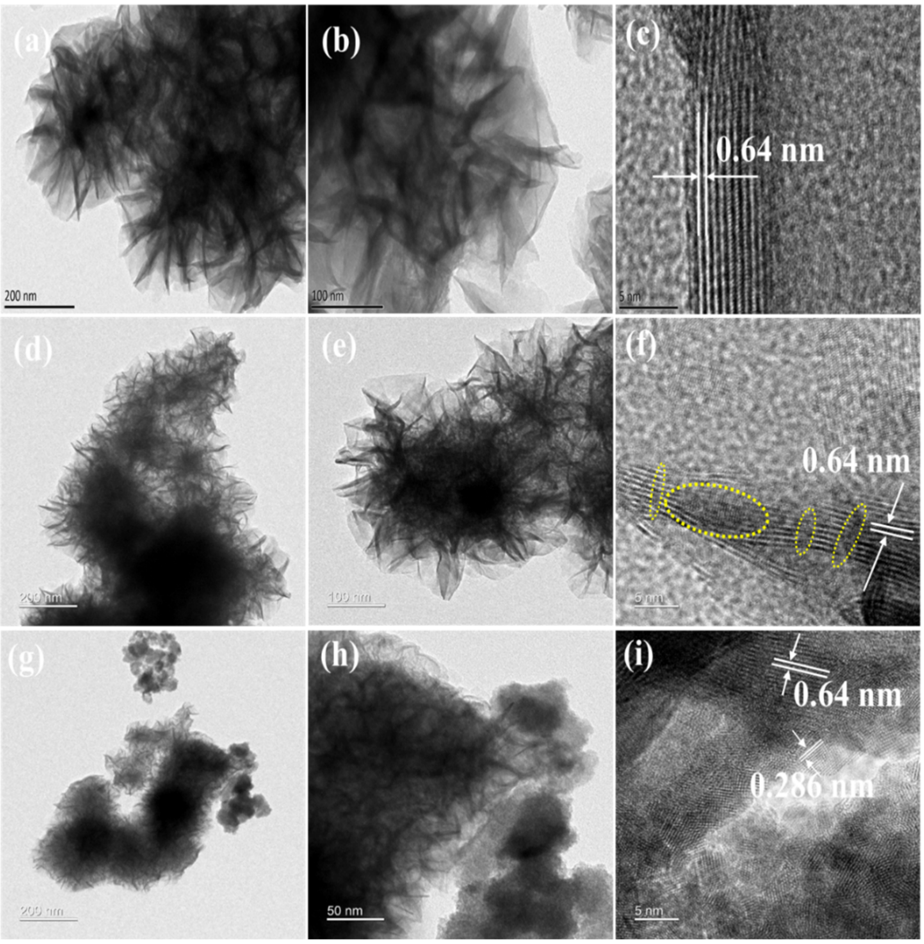

Figure 3. TEM and HRTEM images of (**a**–**c**) MnO_2-b, (**d**–**f**) MCS-1 and (**g**–**i**) MCS-2 samples.

3.2. Physicochemical Properties and Surface States

The influence of $CaSn(OH)_6$ modification on the redox behavior of the catalysts was evaluated by H_2-TPR (Figure 4a). All profiles exhibit a major reduction peak centered around 250 °C, corresponding to the sequential reduction of MnO_2 (δ-$MnO_2 \rightarrow Mn_2O_3/Mn_3O_4 \rightarrow MnO$). Notably, compared to pristine MnO_2-b, the MCS-1 catalyst displays a significantly enlarged reduction peak area. This quantitative increase indicates a higher concentration of reducible surface oxygen species, suggesting that the *in-situ* modification activates the Mn-O bonds, making them more susceptible to reduction.

To further probe the mobility of oxygen species—a critical parameter for oxidation reactions following the Mars-van Krevelen mechanism—O_2-TPD was performed (Figure 4b). The desorption profiles are deconvoluted into three regions: surface-adsorbed oxygen (<300 °C), sub-surface lattice oxygen (300–600 °C), and bulk lattice oxygen (>600 °C). A crucial finding is observed in the high-temperature region: the desorption peak temperature for bulk lattice oxygen in MCS-1 is distinctly lower than that of MnO_2-b and MCS-2. This shift to a lower temperature signifies significantly enhanced lattice oxygen mobility. It implies that lattice oxygen in MCS-1 can migrate from the bulk to the surface more energetically, acting as an efficient “oxygen pump” [34] to replenish surface active sites consumed during HCHO oxidation.

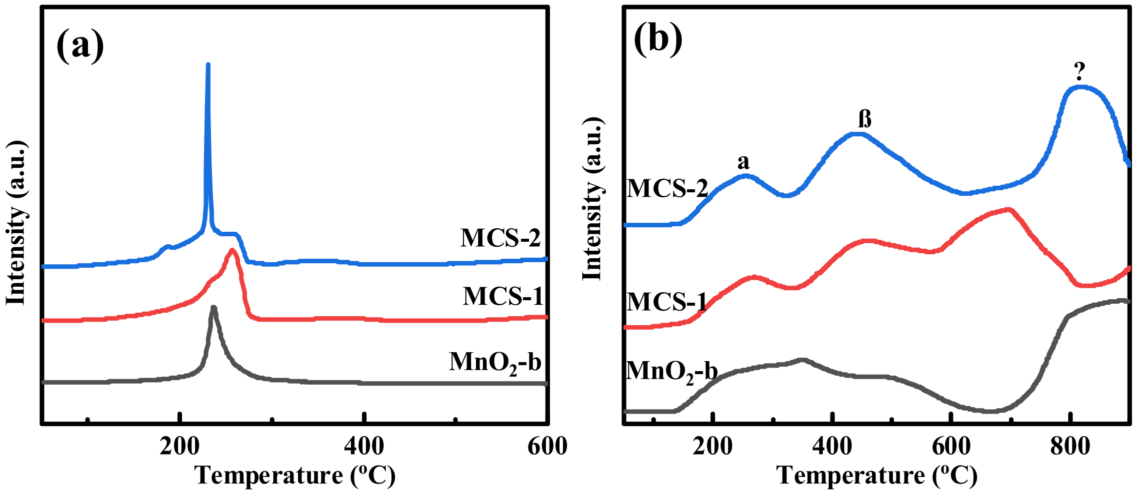

Figure 4. (**a**) H_2-TPR and (**b**) O_2-TPD profiles of different samples.

XPS analyses were conducted to determine the surface elemental states (Figure 5). The survey spectra (Figure 5a) confirm the presence of Mn, O, and K in all samples, with Sn detected exclusively in the MCS-2 composite, consistent with the phase separation observed in SEM/XRD. The Mn $2p_{3/2}$ spectra (Figure 5b) were fitted into two components: Mn^{3+} (641.8 eV) and Mn^{4+} (643.1 eV) [35]. The presence of Mn^{3+} is intrinsically linked to the charge compensation for oxygen vacancies (Vo), following the reaction:

$$4Mn^{4+} + O_2^{-} \rightarrow 4Mn^{4+} + 2e^{-}/Vo + 0.5O_2 \rightarrow 2Mn^{4+} + 2Mn^{3+} + Vo + 0.5O_2 \quad (2)$$

As summarized in Table 1, the Mn^{3+}/Mn^{4+} molar ratio follows the order: MCS-1 (1.71) > MCS-2 (1.66) > MnO_2-b (1.51). The highest Mn^{3+} content in MCS-1 provides solid evidence for the highest concentration of oxygen vacancies, which corroborates the EPR results. This conclusion is further supported by the Mn 3s spectra (Figure 5d), where MCS-1 exhibits the lowest Average Oxidation State (AOS) of 3.68, compared to 3.80 for MCS-2 and 3.93 for MnO_2-b.

The O 1s spectra (Figure 5c) reveal two oxygen species: lattice oxygen (O_{latt}, 529.0 eV) and surface-adsorbed oxygen (O_{ads}, 531.0 eV) [36]. Interestingly, the O_{ads}/O_{latt} ratio is highest for MCS-2 (1.04) and lowest for MCS-1 (0.29). This apparent anomaly in MCS-2 is attributed to the abundant hydroxyl groups inherently present on the surface of the mechanically mixed $CaSn(OH)_6$ cubes. The higher O_{ads}/O_{latt} ratio over MCS-2 sample may result from the mechanical mixture of $CaSn(OH)_6$ and δ-MnO_2. More $CaSn(OH)_6$ was encapsulated by δ-MnO_2 in MCS-1 sample due to its *in-situ* incorporation, resulting in lower O_{ads}/O_{latt} ratio. Although MCS-1 shows a lower O_{ads} ratio, its superior catalytic performance (discussed later) suggests that the intrinsic lattice oxygen mobility (evidenced by O_2-TPD) and oxygen vacancies (evidenced by Mn^{3+} ratio) are the dominant drivers for HCHO oxidation, rather than the simple abundance of surface hydroxyls derived from physical mixing.

Table 1. The surface atomic ratio of Mn and O element estimated by XPS analysis.

Samples	Mn^{3+} (%)	Mn^{4+} (%)	Mn^{3+}/Mn^{4+}	O_{latt} (%)	O_{ads} (%)	O_{ads}/O_{latt}	AOS
MnO_2-b	60.1	39.9	1.51	66.5	33.5	0.50	3.93
MCS-1	63.1	36.9	1.71	77.4	22.6	0.29	3.68
MCS-2	62.4	37.6	1.66	49.1	50.9	1.04	3.80

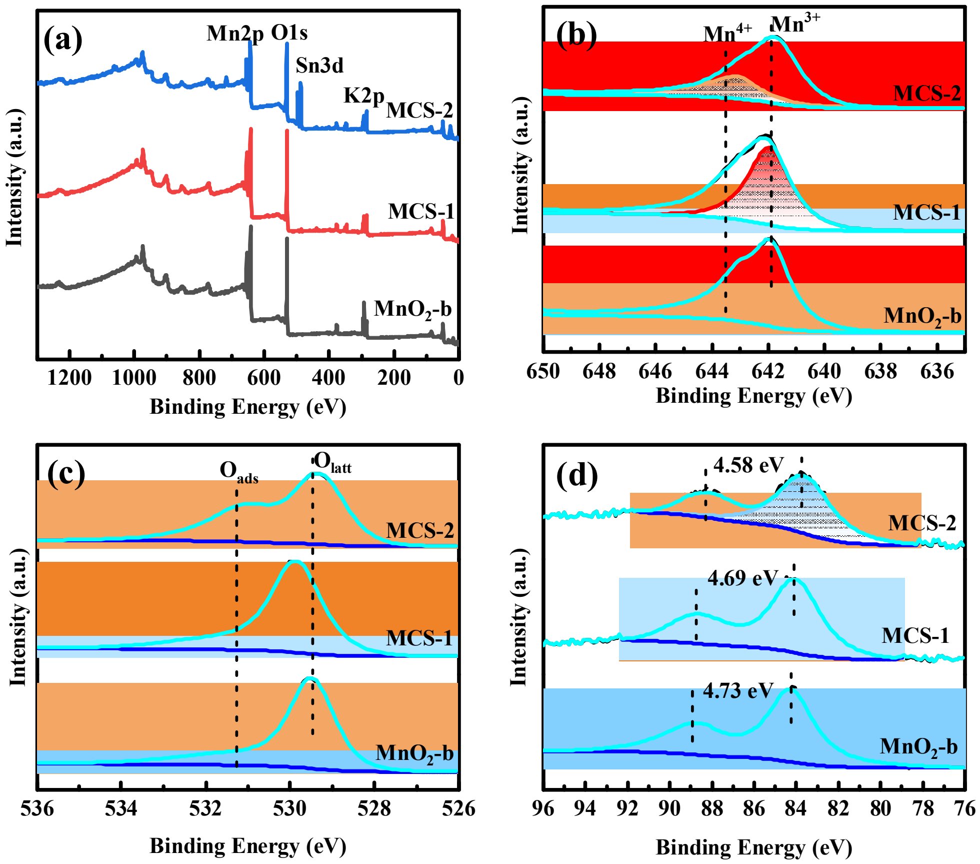

Figure 5. XPS spectra of different catalysts: (**a**) Survey, (**b**) Mn2p3/2, (**c**) O1s and (**d**) Mn 3s.

3.3. Catalytic Performance Evaluation

The catalytic performance of the synthesized samples for HCHO oxidation was evaluated at room temperature (30 °C). As illustrated in Figure 6a, all catalysts exhibit a high initial HCHO removal efficiency (~95%), primarily driven by surface adsorption and the reaction with abundant initial active species1. However, a distinct divergence in performance is observed as the reaction proceeds. The pristine MnO_2-b suffers from rapid deactivation, with the removal efficiency plummeting below 80% after 300 min, indicating the swift accumulation of intermediates and the blockage of active sites. In sharp contrast, the modified catalysts exhibit significantly enhanced durability. Notably, the *in-situ* modified MCS-1 demonstrates the most superior performance, maintaining a removal efficiency above 95% for 260 min and retaining >80% efficiency even after 380 min. Crucially, MCS-1 outperforms the physically mixed MCS-2, confirming that the intimate contact and lattice defects induced by the *in-situ* synthesis—rather than the simple physical presence of $CaSn(OH)_6$—are the key drivers for the enhanced catalytic longevity.

The stability of the optimal MCS-1 catalyst was further assessed through four consecutive reaction cycles (Figure 6b). Each cycle was conducted for a fixed duration of 370 min under identical reaction conditions. The catalyst exhibits excellent stability during the first three cycles, with no apparent loss in activity. Although a slight decline is observed in the fourth cycle (dropping to 80% after 240 min), the overall performance highlights the robustness of the defect-rich structure.

Environmental humidity is a critical parameter governing indoor HCHO abatement. The effect of relative humidity (RH) on the catalytic activity of MnO_2-b and MCS-1 was investigated at RH levels of 20%, 50%, and 80% (Figure 6c). Generally, HCHO oxidation follows a volcano-type dependence on humidity. At high humidity

(RH = 80%), both catalysts suffer from activity loss due to the competitive adsorption between excessive water molecules and HCHO on the active sites.

However, under low-humidity conditions (RH = 20%), a remarkable difference is observed. The activity of pristine MnO_2-b deteriorates rapidly because the scarcity of water vapor hinders the regeneration of surface hydroxyls, which are essential for desorbing formate intermediates. Strikingly, the MCS-1 catalyst retains over 80% efficiency for 300 min under these moisture-deficient conditions. This exceptional low-humidity tolerance is directly attributed to the enhanced lattice oxygen mobility in MCS-1 (as evidenced by O_2-TPD). The mobile lattice oxygen can spontaneously migrate to the surface to participate in the oxidation cycle, thereby reducing the reaction's strict dependence on external water molecules for oxygen replenishment. This result validates that the *in-situ* $CaSn(OH)_6$ modification strategy effectively expands the operational humidity window of δ-MnO_2 for practical applications.

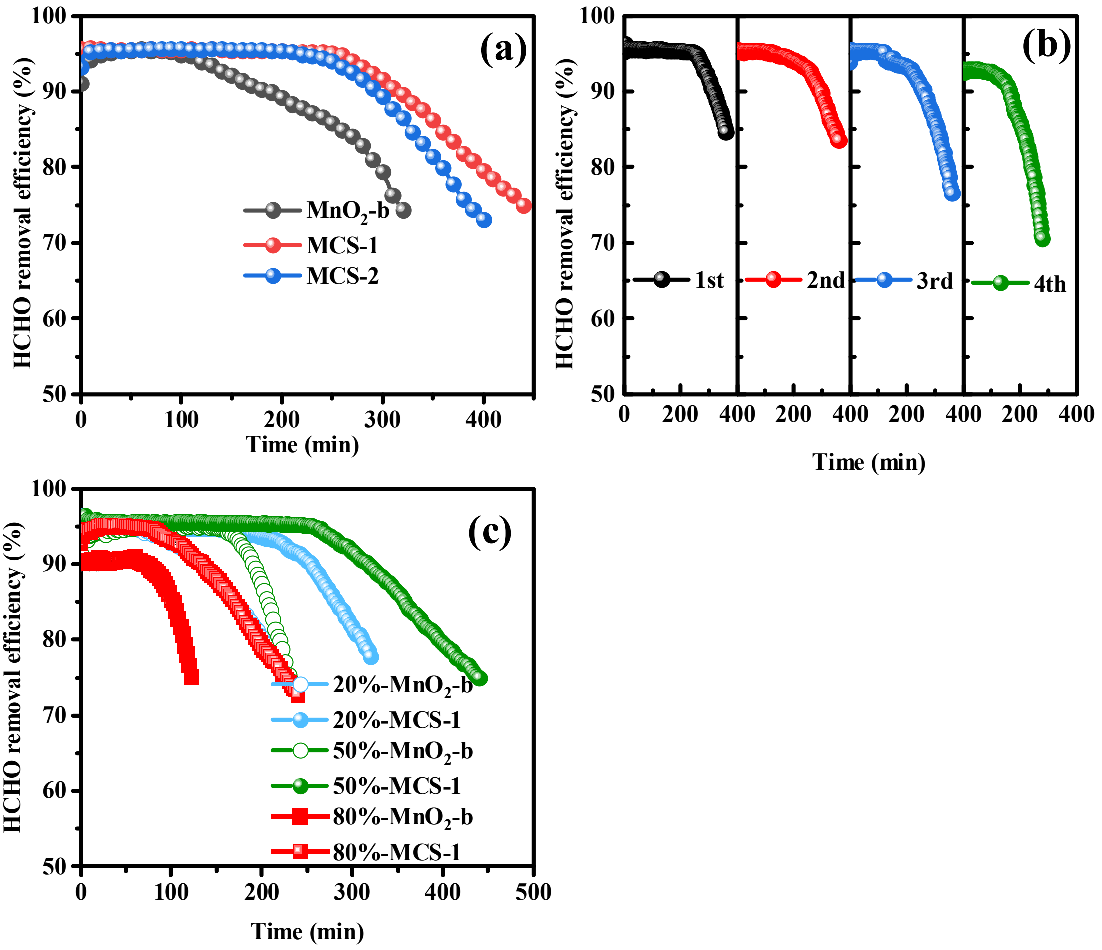

Figure 6. (**a**) HCHO removal efficiency with the rise of time over different samples, (**b**) stability of MCS-1 sample and **(c)** catalytic activity of MnO_2-b and MCS-1 samples under different humidity conditions.

3.4. In-Situ DRIFTS Analysis and Reaction Mechanism

To elucidate the reaction pathway and the role of $CaSn(OH)_6$ modification in suppressing catalyst deactivation, *in-situ* DRIFTS measurements were performed (Figure 7). Upon introducing HCHO, the spectrum of pristine MnO_2-b (Figure 7a) rapidly evolves distinct absorption bands. The peak centered at 1103 cm^{-1} is ascribed to the ν(C–O) stretching vibration of dioxymethylene (DOM), a primary intermediate formed via HCHO adsorption. The bands at 1413/1549 cm^{-1} and 1256/1630 cm^{-1} are assigned to the asymmetric/symmetric stretching vibrations of formate ($HCOO^-$) and carbonate (CO_3^{2-}) species, respectively [37]. The accumulation of these robust intermediates, particularly carbonates, is widely recognized as the primary cause of active site blockage and catalyst poisoning.

In striking contrast, the MCS-1 catalyst (Figure 7b) exhibits a similar spectral pattern but with significantly attenuated peak intensities. Specifically, the characteristic bands for formate (1439, 1600 cm^{-1}) and carbonate (1349, 1666 cm^{-1}) are much weaker compared to MnO_2-b. This reduced intensity does not imply lower activity;

rather, it indicates the rapid turnover and timely desorption of surface intermediates. The enhanced lattice oxygen mobility in MCS-1 facilitates the deep oxidation of stubborn formate/carbonate species into gaseous CO_2, preventing their accumulation on the surface. Furthermore, the FTIR spectra (Figure 7c) reveal that MnO_2-b has a stronger affinity for water adsorption than MCS-1. This excessive hydrophilicity in MnO_2-b exacerbates the competitive adsorption between water and HCHO molecules, whereas the modified surface of MCS-1 mitigates this issue, maintaining high availability of active sites.

Based on the comprehensive characterizations and *in-situ* DRIFTS results, a plausible Mars-van Krevelen (MvK) mechanism for HCHO oxidation over the defect-rich MCS-1 catalyst is proposed (Figure 7d). The gaseous HCHO molecules are first adsorbed on catalyst surface and react with surface active oxygen species into DOM intermediates. Then, the DOM species are rapidly oxidized into unstable formate and subsequently mineralized into carbonate species, finally decomposing into CO_2 and H_2O. During this process, surface active oxygen species are consumed. The transformation of formate or carbonate species into CO_2 and H_2O is reported as the rate-determining step [19]. The abundant oxygen vacancies (Vo) induced by the *in-situ* $CaSn(OH)_6$ modification act as activation centers. They capture and activate gaseous oxygen (O_2) to form reactive superoxide or peroxide species (O_2^-, O^-), which then refill the oxygen vacancies and regenerate surface lattice oxygen.

Consequently, the superior performance of MCS-1 stems from a synergistic effect: the high density of oxygen vacancies ensures the continuous supply of active oxygen species, while the enhanced lattice oxygen mobility accelerates the decomposition of intermediates. This efficient "adsorption-oxidation-regeneration" cycle effectively prevents the poisoning of active sites, enabling robust HCHO elimination even under harsh, low-humidity conditions.

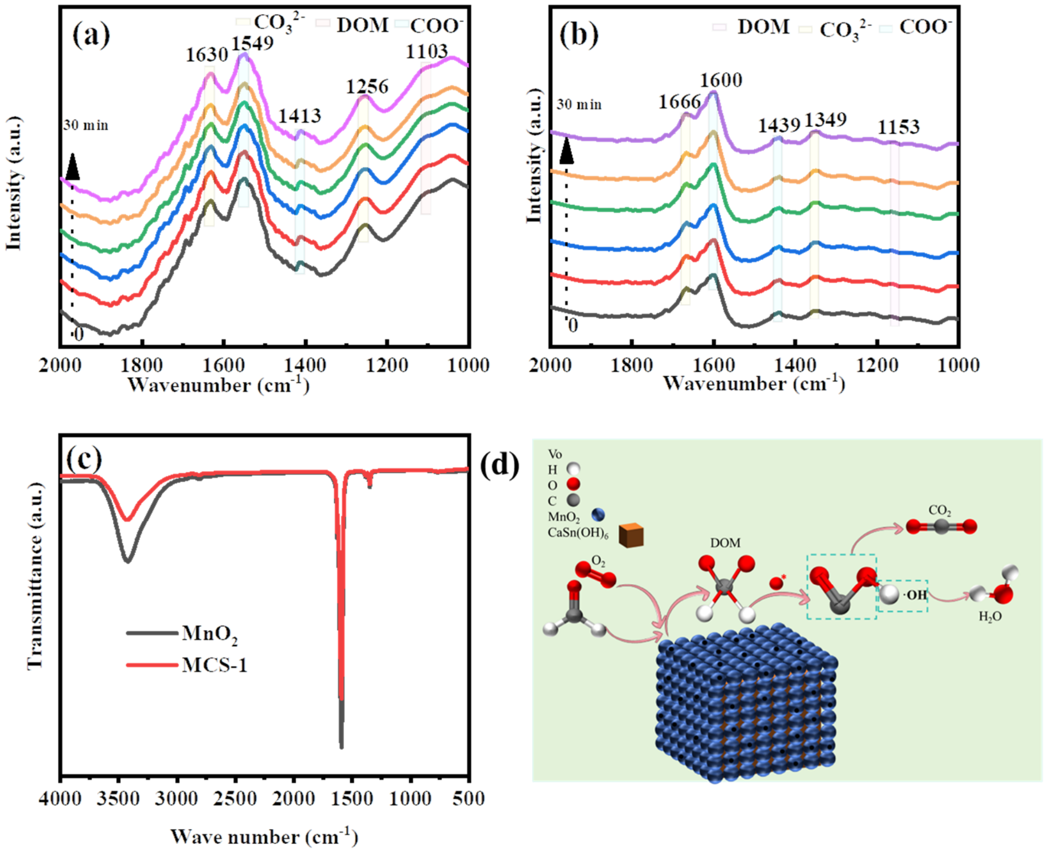

Figure 7. *In-situ* DRIFTS spectra of (**a**) MnO_2-b and (**b**) MCS-1 samples, (**c**) FTIR spectra of MnO_2-b and MCS-1 samples, (**d**) Proposed reaction mechanism of HCHO oxidation on MCS-1 sample.

4. Conclusions

In summary, the catalytic robustness of layered δ-MnO_2 for formaldehyde oxidation was significantly elevated through a facile *in-situ* $CaSn(OH)_6$ modification strategy. Unlike simple physical mixing, this *in-situ* approach effectively induced a high concentration of surface oxygen vacancies and lattice distortions within the MnO_2 framework, as confirmed by EPR and Raman analyses. Experimental and mechanistic investigations revealed that these engineered defects play a pivotal dual role: they not only serve as active sites for molecular oxygen activation but, more critically, accelerate the mobility of bulk lattice oxygen. Consequently, the optimized catalyst (MCS-1) exhibited exceptional tolerance to moisture-deficient environments (RH = 20%), overcoming the longstanding bottleneck of deactivation caused by hydroxyl depletion and maintaining a high HCHO removal efficiency of over 95% for extended periods. The superior performance is fundamentally attributed to the rapid regeneration of surface active oxygen and the timely desorption of carbonate intermediates, which prevents active site poisoning. By elucidating the dynamic interplay between lattice oxygen mobility and intermediate evolution, this work provides a promising defect-engineering protocol for developing durable manganese-based catalysts tailored for real-world indoor air purification under harsh environmental conditions.

Author Contributions

R.F.: Writing—original draft, Resources, Investigation. Q.L.: Investigation, Data curation. G.L.: Investigation, Formal analysis, Data curation. X.L.: Data curation, Conceptualization. H.M.: Writing—review & editing, Supervision, Funding acquisition, Formal analysis. H.H.: Supervision, Investigation. All authors have read and agreed to the published version of the manuscript.

Funding

The authors gratefully acknowledge the financial supports from the National Natural Science Foundation of China (No. 51908091, No. 52200122), the Natural Science Foundation of Chongqing (No. CSTB2024NSCQ-MSX0464, No. CSTB2025NSCQ-GPX0136), the Science and Technology Research Project of Chongqing Education Commission (No. KJQN202300821, No. KJQN202500841) and the Start-up Foundation of High-level Talents in Chongqing Technology and Business University (No.1856044).

Data Availability Statement

Data will be made available on request.

Conflicts of Interest

The authors declare no conflict of interest.

Use of AI and AI-Assisted Technologies

No AI tools were utilized for this paper.

References

1. Ait Benhamou, A.; Abid, L.; Calvez, I.; et al. Advances in lignin chemistry, bonding performance, and formaldehyde emission reduction in lignin-based urea-formaldehyde adhesives: A Review. *ChemSusChem* **2025**, *18*, e202500491.
2. Liu, J.; Wang, Y.; Ji, W. Formaldehyde pollution characteristics and health risk assessment of workers during indoor renovation. *Build. Environ.* **2026**, *287*, 113853.
3. Chen, L.; Yang, N.; Li, K.; et al. Dynamic evolution of Mn–O site and ROS formation in room-temperature formaldehyde oxidation over phase-dependent MnO_2. *Environ. Sci. Technol.* **2025**, *59*, 24092–24102.
4. Khoshakhlagh, A.H.; Mohammadzadeh, M.; Sicard, P.; et al. Human exposure to formaldehyde and health risk assessment: A 46-year systematic literature review. *Environ. Geochem. Health* **2024**, *46*, 206.
5. Shan, C.; Wang, Y.; Li, J.; et al. Recent advances of VOCs catalytic oxidation over spinel oxides: Catalyst design and reaction mechanism. *Environ. Sci. Technol.* **2023**, *57*, 9495–9514.
6. Zhao, J.; Xi, W.; Tu, C.; et al. Catalytic oxidation of chlorinated VOCs over Ru/Ti_xSn_{1-x} catalysts. *Appl. Catal. B. Environ.* **2020**, *263*, 118237.
7. Chen, R.; Sun, Z.; Hardacre, C.; et al. The current status of research on the catalytic oxidation of formaldehyde. *Catal. Rev.* **2024**, *66*, 1028–1083.
8. Liu, X.; Lu, T.; Jiao, X.; et al. Formaldehyde ambient-temperature decomposition over Pd/Mn_3O_4–MnO driven by active sites' self-tandem catalysis. *Environ. Sci. Technol.* **2024**, *58*, 1752–1762.
9. Vikrant, K.; Chung, M.W.; Boukhvalov, D.W.; et al. A platinum ensemble catalyst for room-temperature removal of formaldehyde in the air. *Chem. Eng. J.* **2023**, *475*, 146007.
10. Qin, X.; Chen, X.; Chen, M.; et al. Highly efficient Ru/CeO_2 catalysts for formaldehyde oxidation at low temperature and the mechanistic study. *Catal. Sci. Technol.* **2021**, *11*, 1914–1921.

11. Sun, X.; Wang, Y.; Cui, J.; et al. Noble-metal-based catalysts on a scale from nanoparticles to subnanoclusters and single atoms for formaldehyde oxidation at room temperature: A review. *ACS Appl. Nano. Mater.* **2024**, *7*, 3546–3563.
12. Bai, B.; Qiao, Q.; Li, J.; et al. Progress in research on catalysts for catalytic oxidation of formaldehyde. *Chin. J. Catal.* **2016**, *37*, 102–122.
13. Shi, L.; Zhou, X.; Guo, Y.; et al. Designing of 3D MnO_2-graphene catalyst on sponge for abatement temperature removal of formaldehyde. *J. Hazard. Mater.* **2023**, *441*, 129836.
14. Wang, M.; Hong, X.; Chen, J.; et al. Two-step hydrothermal synthesis of highly active MnO_x-CeO_2 for complete oxidation of formaldehyde. *Chem. Eng. J.* **2022**, *440*, 135854.
15. Zhang, X.; Guo, L.; Wang, Y.; et al. Y single atoms boost MnO_2 for efficient ambient formaldehyde catalytic oxidation. *Sep. Purif. Technol.* **2025**, *362*, 131962.
16. Fang, R.; Huang, X.; Luo, X.; et al. Excellent stability for catalytic oxidation formaldehyde over defective δ-MnO_2 nanoparticles at room temperature. *J. Environ. Chem. Eng.* **2023**, *11*, 109064–109071.
17. Chen, L.; Li, K.; Xue, T.; et al. Efficient and durable oxidation removal of formaldehyde over layered double hydroxide catalysts at room temperature. *Environ. Sci. Technol.* **2024**, *58*, 10378–10387.
18. Wu, Y.; Guo, Q.; Liu, H.; et al. Effect of Fe doping on the surface properties of δ-MnO_2 nanomaterials and its decomposition of formaldehyde at room temperature. *J. Environ. Chem. Eng.* **2022**, *10*, 108277.
19. Ji, J.; Lu, X.; Chen, C.; et al. Potassium-modulated δ-MnO_2 as robust catalysts for formaldehyde oxidation at room temperature. *Appl. Catal. B. Environ.* **2020**, *260*, 118210–118221.
20. Ma, C.; Yang, C.; Wang, B.; et al. Effects of H_2O on HCHO and CO oxidation at room-temperature catalyzed by MCo_2O4 (M = Mn, Ce and Cu) materials. *Appl. Catal. B. Environ.* **2019**, *254*, 76–85.
21. Li, R.; Huang, Y.; Zhu, Y.; et al. Enhancing oxygen activation ability by composite interface construction over a 2D Co_3O_4-based monolithic catalyst for toluene oxidation. *Environ. Sci. Technol.* **2024**, *58*, 14906–14917.
22. Ma, H.; Yang, W.; Tang, H.; et al. Enhance the stability of oxygen vacancies in $SrTiO_3$ via metallic Ag modification for efficient and durable photocatalytic NO abatement. *J. Hazard. Mater.* **2023**, *452*, 131269.
23. Xu, C.; Lu, S.; Chen, Y.; et al. Ce-MOFs derived spindle-like MnO_2-CeO_2 heterostructures for enhanced catalytic oxidation of formaldehyde. *J. Environ. Chem. Eng.* **2026**, *14*, 122226.
24. Xing, G.; Liu, X.; Jia, Y.; et al. Oxygen vacancy–rich K-Mn_3O_4@CeO_2 catalyst for efficient oxidation degradation of formaldehyde at near room temperature. *J. Colloid. Interf. Sci.* **2025**, *677*, 417–428.
25. Chen, B.; Shi, C.; Crocker, M.; et al. Catalytic removal of formaldehyde at room temperature over supported gold catalysts. *Appl. Catal. B. Environ.* **2013,** *132–133*, 245–255.
26. Zheng, Y.; Fu, K.; Yu, Z.; et al. Oxygen vacancies in a catalyst for VOCs oxidation: Synthesis, characterization, and catalytic effects. *J. Mater. Chem. A.* **2022**, *10*, 14171–14186.
27. Li, X.; Wang, Y.; Chen, D.; et al. A highly dispersed Pt/copper modified-MnO_2 catalyst for the complete oxidation of volatile organic compounds: The effect of oxygen species on the catalytic mechanism. *Green. Energy. Environ.* **2023**, *8*, 538–547.
28. Wang, H.; Dong, X.; Tang, R.; et al. Selective breakage of CH bonds in the key oxidation intermediates of gaseous formaldehyde on self-doped CaSn(OH)6 cubes for safe and efficient photocatalysis. *Appl. Catal. B. Environ.* **2020**, *277*, 119214.
29. Do, S.-B.; Lee, S.-E.; Kim, T.-O. Oxidative decomposition with PEG-MnO_2 catalyst for removal of formaldehyde: Chemical aspects on HCHO oxidation mechanism. *Appl. Surf. Sci.* **2022**, *598*, 153773.
30. Huang, Y.; Liu, Y.; Wang, W.; et al. Oxygen vacancy–engineered δ-MnO_x/activated carbon for room-temperature catalytic oxidation of formaldehyde. *Appl. Catal. B. Environ.* **2020**, *278*, 119294.
31. Ma, H.; Li, W.; Liu, B.; et al. Oxygen vacancies induced intrinsic electric field attenuation for superior molecular oxygen activation and NO oxidation. *Chem. Eng. J.* **2025**, *505*, 159421.
32. Zhu, G.; Zhu, J.; Jiang, W.; et al. Surface oxygen vacancy induced α-MnO_2 nanofiber for highly efficient ozone elimination. *Appl. Catal. B. Environ.* **2017**, *209*, 729–737.
33. Liu, T.; Ma, X.; Yang, L.; et al. Highly enhanced photocatalytic activity of $CaSn(OH)_6$ through tuning $CaSn(OH)_6/SnO_2$ heterostructural interaction and optimizing Fe^{3+} doping concentration. *Appl. Catal. B. Environ.* **2017**, *217*, 256–264.
34. Dong, C.; Yang, C.; Ren, Y.; et al. Local electron environment regulation of spinel $CoMn_2O_4$ induced effective reactant adsorption and transformation of lattice oxygen for toluene oxidation. *Environ. Sci. Technol.* **2023**, *57*, 21888–21897.
35. Wang, C.; Chen, J.; Li, Q.; et al. Unveiling the position effect of Ce within layered MnO_2 to prolong the ambient removal of indoor HCHO. *Environ. Sci. Technol.* **2023**, *57*, 4598–4607.
36. Xie, J.; Zhang, X.; Zhang, X.; et al. Substitutional C and interstitial N in MnO_2/NC catalysts enable high performance of formaldehyde oxidation at room temperature. *J. Environ. Chem. Eng.* **2023**, *11*, 111346.
37. Wang, J.; Li, J.; Jiang, C.; et al. The effect of manganese vacancy in birnessite-type MnO_2 on room-temperature oxidation of formaldehyde in air. *Appl. Catal. B. Environ.* **2017**, *204*, 147–155.